3.1. Introduction

The perovskite oxide materials having high dielectric constants are mostly used for the miniaturization of electronic devices [Cava (2001), Singh *et al.* (2014), Bhalla *et al.* (2000)]. Calcium copper titanate $CaCu_3Ti_4O_{12}$ (CCTO) has complex perovskite structure having dielectric constant (~10^4) which is constant over a wide range of temperature 100 - 600 K [Xue *et al*. (2015), Mallmann *et al*. (2015), Wang *et al*. (2014)]. This anomalous dielectric behavior of CCTO was explained by internal barrier layer capacitor (IBLC) model which shows the existence of semiconducting grains and insulating grain boundaries supported by impedance spectroscopy [Sinclair *et al.* (2002), Wu *et al*. (2005)]. It is reported that hexagonal perovskite oxide $Ba_4YMn_3O_{11.5-\delta}$ (BYMO), also shows very interesting dielectric properties similar to CCTO [Liu *et al*. (2009), Subramanian *et al*. (2000)]. Besides CCTO ceramics, few materials such as doped NiO [Wu *et al*. (2002)], $La_{2x}Sr_xNiO_4$ (x= 1/3 or 1/8) [Krohns *et al*. (2009)] and $(In_{0.5}Nb_{0.5})_xTi_{1-x}O_2$ (x= 0.05, 10, 20%) [Hu *et al*. (2013)] which are investigated recently, also shows very high dielectric constant and low dielectric loss [Krohns *et al*. (2009)]. BYMO shows ferroelectric properties because of different oxidation states of $Mn^{3+/4+}$ responsible for electronic heterogeneity and extent of polarization. It is an established fact that high dielectric constant is the main key source for the presence of ferroelectricity in $BaTiO_3$ ceramic. When the external electric field is applied on $BaTiO_3$ the domains are aligned in grains thus orientation of titanium atom shifts in direction of applied field which creates the polarization [Haertling (1999)]. Such alignment of domains was absent at grain boundary which is responsible for the electrical properties of $BaTiO_3$. The ferroelectric, leakage, dielectric, piezoelectric, magnetic and magneto electric properties were investigated for $BiFeO_3/Bi_4Ti_3O_{12}$ composite film which possess strong magneto electric effect at room

temperature [Chen *et al*. (2016a)]. The excellent ferroelectric properties of $Bi_{0.5}(Na_{0.85}K_{0.15})_{0.5}TiO_3$ film were obtained due to the well-defined domain structure and its switching [Chen *et al*. (2016b)]. The unique structure of BYMO consists of MnO_6 and YO_6 octahedra linked by either face sharing or corner sharing by oxide linkage. Since the physical, ferroelectric, dielectric and electrical properties may depend on microstructure and the processing route. Now a day, the sol gel auto-combustion method has been established as a popular synthetic technique for materials preparation [Aruna and Muksyan (2008), Singh *et al*. (2014)]. In the present chapter, BYMO was synthesized for the first time using sol-gel combustion and measured ferroelectric property. This technique provides the advantages of the sol-gel chemistry with the combustion process, resulting homogeneous crystalline powder of BYMO ceramic at lower sintering temperature and small sintering time duration than the other synthesis process reported earlier [Kuang *et al*. (2012), Kuang *et al*. (2006), Barbier *et al*. (2012)]. The elaboration of thermo gravimetric, microstructural, dielectric, ferroelectric and impedance spectroscopic analysis of BYMO are also reported in this chapter.

3.2. Experimental

3.2.1. Materials synthesis:

BYMO ceramic was prepared by a wet chemical route. The chemicals used are of analytical grade, $Ba(NO_3)_2$ (99 % Merck India), $Y(NO_3)_3$ $6H_2O$, (99 % Himedia India), $Mn(CH_3COO)_2$ $4H_2O$ and glycine (99 % Merck India) were used without any further purification. Standard aqueous solutions of metal nitrates/acetate were prepared using double distilled water with their calculated stoichiometric amounts of Ba^{2+}, Y^{3+} and Mn^{3+} metal ions. The stoichiometric amount of glycine equivalent to metal ions was added to the solution. The solution was heated with constant stirring using magnetic stirrer at 70 - 80 ^{0}C to evaporate

water and resulting dry gel was burned with sooty flame. The resulting compound was converted into fine powder using agate and mortar. The obtained fine powder was calcined at 800 ^{0}C for 8 h in an electrical furnace. The calcined powder was mixed with 2 wt % polyvinyl alcohol (PVA) as binder and pressed into cylindrical pellets (10 mm × 1.52 mm) using hydraulic press applying pressure of nearly 4 ~ 5 ton for 60 seconds. The pellets were sintered at 1100 ^{0}C for 12 h in air.

3.2.2. Characterization of synthesized material:

The samples were characterized by TG/DTA (SII 6300 EXSTAR) with the heating rate of 10^{0}C/min, Phase of the samples were analyzed by X-ray powder diffraction with Cu-Kα radiation (λ= 1.54056 Å) (Rigaku miniflex 600) in the range of 2θ ($20^0 \leq 2\theta \leq 80^0$) at the scan rate 4 ^{0}/min.

3.2.3. Microstructural and electrical characterization:

A field emission electron microscopy (FESEM) equipped with an energy dispersive X-ray spectroscopy (EDX) (QUANTA 200 F) was used for determination of microstructure and elemental composition of sintered sample respectively. The particle size and selected area diffraction pattern (SAED) were studied by transmission electron microscopy (TEM) (TECNAI 20 G^2). The capacitance, dielectric loss (tan δ) and conductance variation with temperature and frequency were measured by LCR meter (PSM1735 NumetriQ UK). Hysteresis loop induced by an electric field were carried out on a ferroelectric tester (Automatic PE Loop Tracer Marine India).

3.3. Results and discussion

Figure 3.1 shows the XRD pattern of BYMO ceramic sintered at 1100 ^{0}C for 12 h. All the peaks were indexed with hexagonal structure (JCPDS26-0166). XRD pattern shows the formation of BYMO single phase at relatively lower temperature than earlier reported in literature [Barbier *et al*. (2012)]. The crystallite size (D) was calculated by using Scherrer formula [Culity (2001)] as given in equation (3.1).

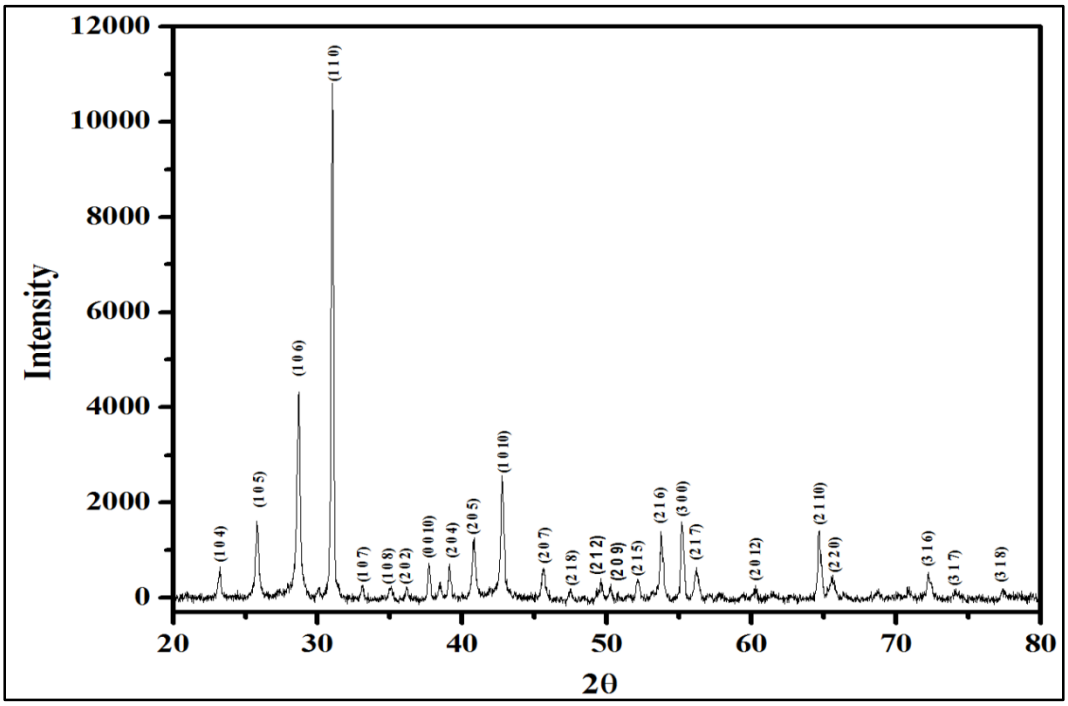

Figure 3.1 X-ray powder diffraction patterns of $Ba_4YMn_3O_{11.5-\delta}$ sintered at 1100 ^{0}C for 12 h

$$D = \frac{k\lambda}{\beta \cos\theta} \qquad (3.1)$$

Where λ is the wavelength of X ray, the constant k value is taken as 0.94, θ is diffraction angle and β represents full width at half maximum (FWHM). The TG/DTG curve of synthesized material was shown in Figure 3.2 which indicates the three major stages of weight loss from ambient temperature to 1100 ^{0}C.

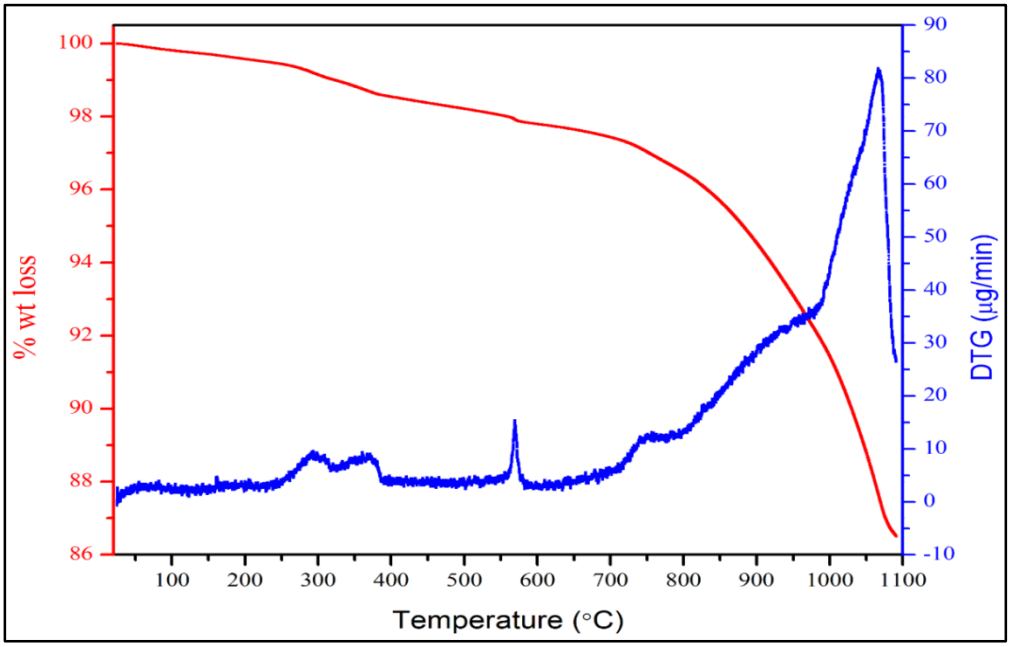

Figure 3.2 Simultaneous TG/ DTG curves for the precursor powder $Ba_4YMn_3O_{11.5-\delta}$

The first weight loss was observed from 250 to 400 ^{0}C due to removal of unreacted glycine molecules. Second peak was observed at 550 to 600 ^{0}C due to decomposition of manganese acetate to Mn_3O_4 and carbon dioxide [Sahoo and Panda (2013)], as given in equation (3.2) third major weight loss from 800 to 1100 ^{0}C indicates thermal decomposition of barium carbonate into barium oxide and carbon dioxide which leads to the formation of final product as mentioned in equation (3.3) and (3.4).

$$3Mn(CH_3COO)_2.4H_2O + 12\frac{1}{2}O_2 \rightarrow Mn_3O_4 + 12CO_2 + 21H_2O \quad (3.2)$$

$$BaCO_3 \rightarrow BaO + CO_2 \quad (3.3)$$

$$4BaO + Mn_3O_4 + \frac{1}{2}Y_2O_3 + O_2 \rightarrow Ba_4YMn_3O_{11.5} \quad (3.4)$$

Figure 3.3 shows the bright field TEM image and selected area diffraction (SAED) pattern of BYMO ceramic powder sintered at 1100 ^{0}C for 12 h. Nano crystalline BYMO having particle size of 45 ± 10 nm Figure 3.3 (a). Shows the hexagonal particles are separated by well-defined boundary. Selected area diffraction pattern of the BYMO ceramic is shown in Figure 3.3 (b) which is indexed with the help of ratio of the principle spot spacing and angles between the planes which assist the hexagonal structure of BYMO ceramic [Williams and Carter (2009)]. The zone axis of the material was found to be [1 $\bar{2}$ 1 $\bar{3}$]. The particle size observed by TEM and XRD are listed in Table 3.1.

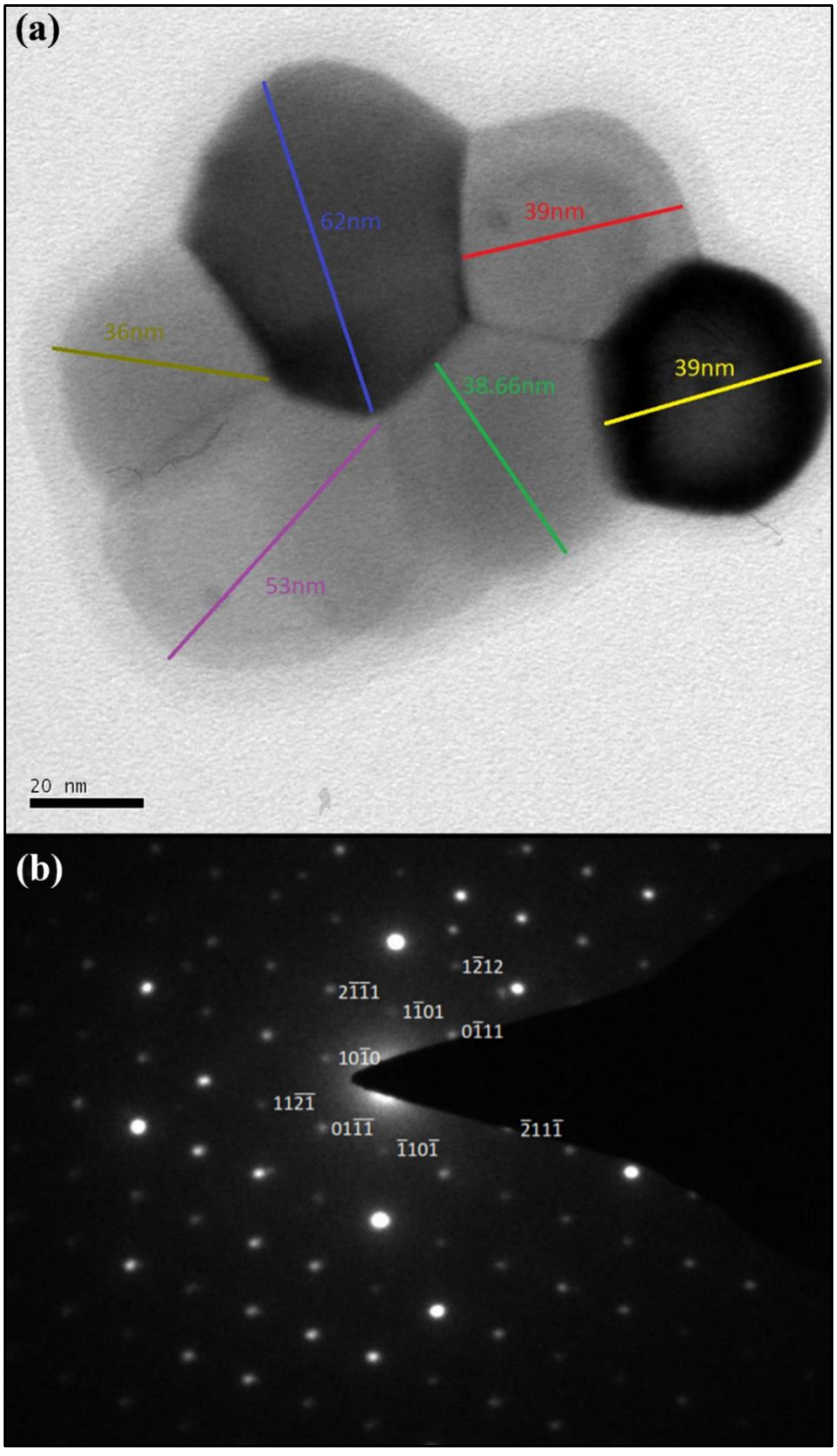

Figure 3.3 (a) Bight field TEM image of $Ba_4YMn_3O_{11.5-\delta}$ **(b)** corresponding selected area electron diffraction (SAED) pattern

Table 3.1 XRD parameters and particle size obtained from XRD and TEM of $Ba_4YMn_3O_{11.5-\delta}$ ceramic

System	2θ (deg)	d (Å)	Rel. Int.	FWHM (deg)	Particle size (nm) XRD	TEM
$Ba_4YMn_3O_{11.5-\delta}$	28.66	3.11	64.45	0.202		
	25.79	3.45	22.8	0.226		
	31.01	2.88	100	0.153	46±10	45±10
	42.35	2.11	37.93	0.186		

It is observed from the table that the average particle size calculated from XRD and particle size obtained from the TEM is almost similar [Mou *et al.* (2014), Wellons *et al*. (2007)] due to particles are delineated by well-defined boundary or loose nanoparticles of ceramic materials and this similar observation was also supported by parallel spot observed in SAED pattern which was sign of single crystal nature of material [Akbari *et al.* (2011)]. The SEM image of BYMO ceramic sintered at 1100 ^{0}C for 12 h is shown in Figure 3.4 (a). The grain size was found in nano-crystalline nature in the range of 80 ± 10 nm. The XRD gives the coherent domain size which could be less than SEM because X ray visualize a part of a grain separated from other part of it which treated as single crystallite whereas in SEM size of complete grain was observed [Gaikwad *et al*. (2014)].

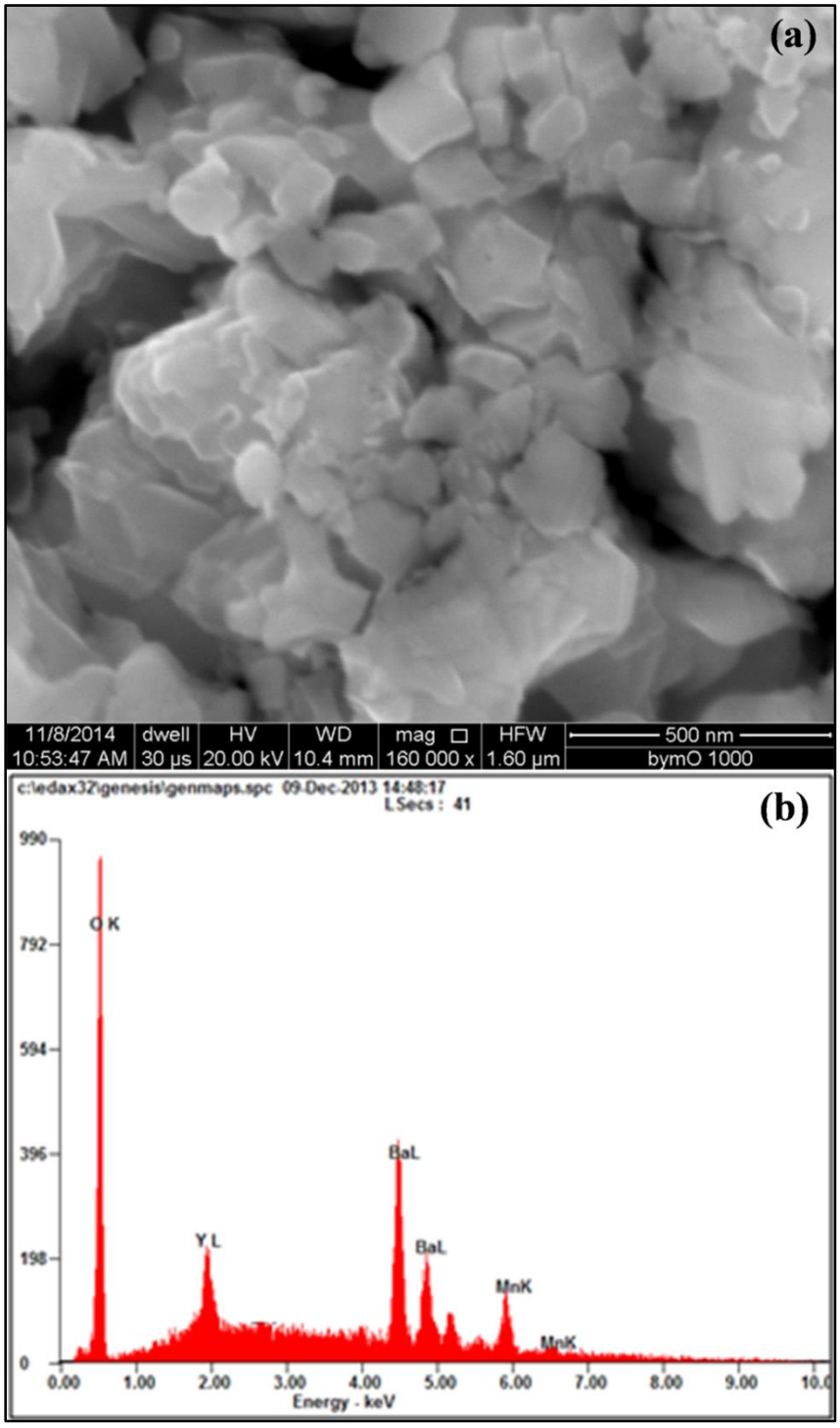

Figure 3.4 (a) SEM micrograph **(b)** EDX spectra of $Ba_4YMn_3O_{11.5-\delta}$

Figure 3.4 (b) shows the EDX spectrum of corresponding SEM image. The spectra show presence of Ba, Y, Mn and O element with atomic percentage 34.32, 4.66, 21.49, and 38.74 respectively, which confirms the purity of material synthesized by represented chemical method. The polarization versus electric field PE hysteresis loops of BYMO ceramic were recorded at different temperatures shown in Figure 3.5. These measurements were carried out at a frequency of 200 Hz. As temperature increases the loop becomes slimmer which indicates evolution process to relaxor ferroelectrics [Huang *et al*. (2015)].

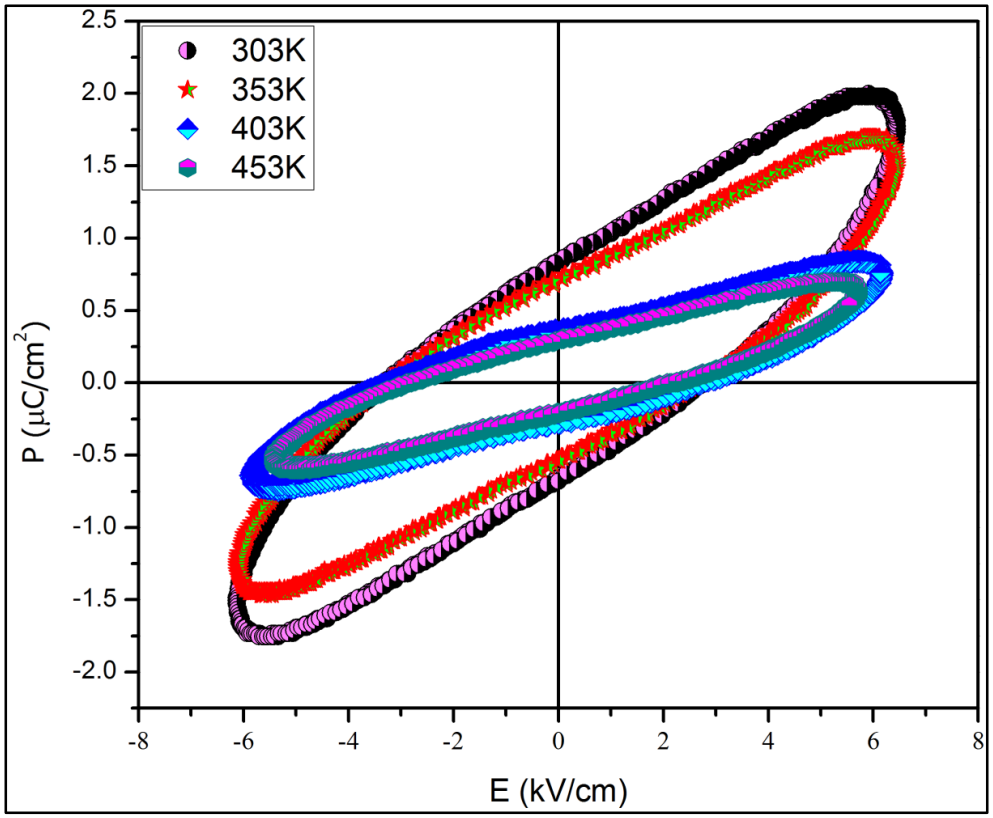

Figure 3.5 Ferroelectric hysteresis PE hysteresis loop for $Ba_4YMn_3O_{11.5-\delta}$ sintered at 1100 ^{0}C for 12 h

At a given electric field corresponding remanent polarization (Pr), coercive electric field (Ec) decreases with temperature. The decrement in polarization with temperature was due to oppose of electric field induced ferroelectric switching of dipoles with increase of temperature [Yadava *et al*. (2016)]. The observed remanent polarization of BYMO ceramics is 0.88, 0.70, 0.41 and 0.25 $\mu C/cm^2$ at 303, 353, 403 and 453 K respectively. The saturation was not observed even applying high electric field the observed curve may be explained by the combined effect of capacitor and resistor joint in parallel (lossy capacitor). The variations of dielectric constant (ε_r) and dielectric loss (tan δ) with temperature at few selected frequencies are shown in Figure 3.6. The slight increase in dielectric constant at high temperature may be due to the polarization of thermally activated charge vacancies and dipoles shown in Figure 3.6 (a). The relaxation peaks of tan δ were observed in the temperature range, 350 - 450 K as shown in Figure 3.6 (b). The intensity of peaks decreases with increasing frequencies. It is also observed that the values of dielectric loss are higher at lower frequency regions as compared to those at higher frequencies.

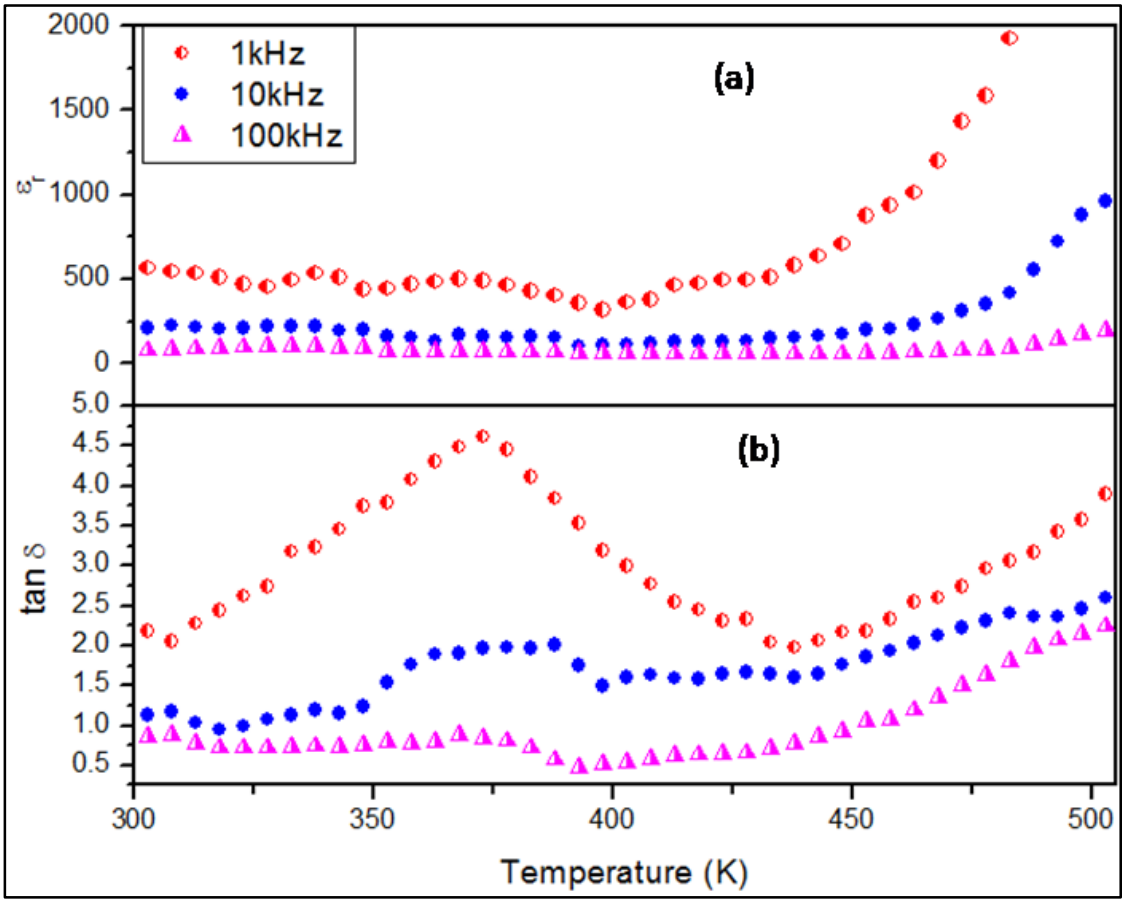

Figure 3.6 Plots of **(a)** dielectric constant (ε_r) and **(b)** dielectric loss (tan δ) Vs temperature for $Ba_4YMn_3O_{11.5-\delta}$ at selected frequency

Thus, the high temperature and low frequency affects the dielectric behavior of BYMO ceramic. The frequency dependent dielectric constant (ε_r) and dielectric loss (tan δ) are shown in Figure 3.7. It is observed from the Figure 3.7 (a) that the dielectric constant gradually increases with decrease in frequency and the increment is prominent in the low frequency region and high temperature which may be explained by the relaxation of dipoles at the grain boundaries and electrode interface effect. Figure 3.7 (b) shows that the dielectric loss and temperature is inversely related to each other.

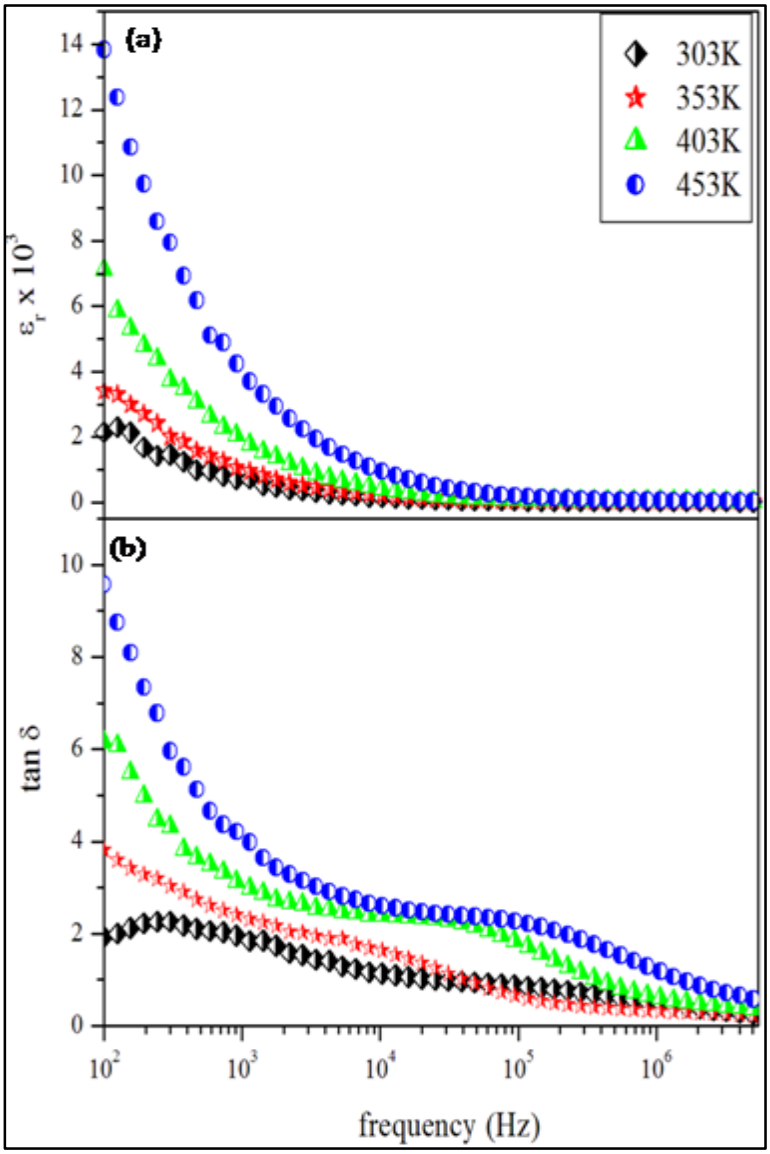

Figure 3.7 Plots of **(a)** dielectric constant (ε_r) **(b)** dielectric loss (tan δ) Vs frequency for $Ba_4YMn_3O_{11.5-\delta}$ at selected temperature

This may be due to relaxation of dipoles at grain boundary [Singh *et al*. (2013)]. The high dielectric loss in the low frequency region may be due to the conduction of oxygen vacancies. These charge vacancies are created by mass diffusion during sintering process [Fang *et al.* (2004)] as given by the equation (3.5);

$$O_o \leftrightarrow \frac{1}{2}O_2 + V_o^{\cdot\cdot} + 2e' \quad (3.5)$$

The electron released in above reaction may be captured by Mn^{4+} or Y^{3+} to produce Mn^{3+} and Y^{2+} respectively as represented by the equation (3.6) and (3.7);

$$2Mn^{4+} + 2e^- \rightarrow 2Mn^{3+} \quad (3.6)$$

$$2Y^{3+} + 2e^- \rightarrow 2Y^{2+} \quad (3.7)$$

The probability of formation of Y^{2+} is negligible as Y^{3+} with $4d^0$ electronic configurations. On the other hand, Mn^{3+} with $3d^4$ configuration is stable due to high crystal field stabilization energy CFSE. The oxygen vacancy and electron transfer from these dipoles can change their orientation due to either hoping of electron between Mn^{4+} and Mn^{3+} or jumping of O^{2-} ions may jump through vacant oxygen sites around MnO_6 octahedra leading to orientation polarization [Singh *et al.* (2014)].

Figure 3.8 shows the plots of AC conductivity as a function of frequency at few selected temperatures. It is observed from the figure that the AC conductivity depends on frequency and temperature.

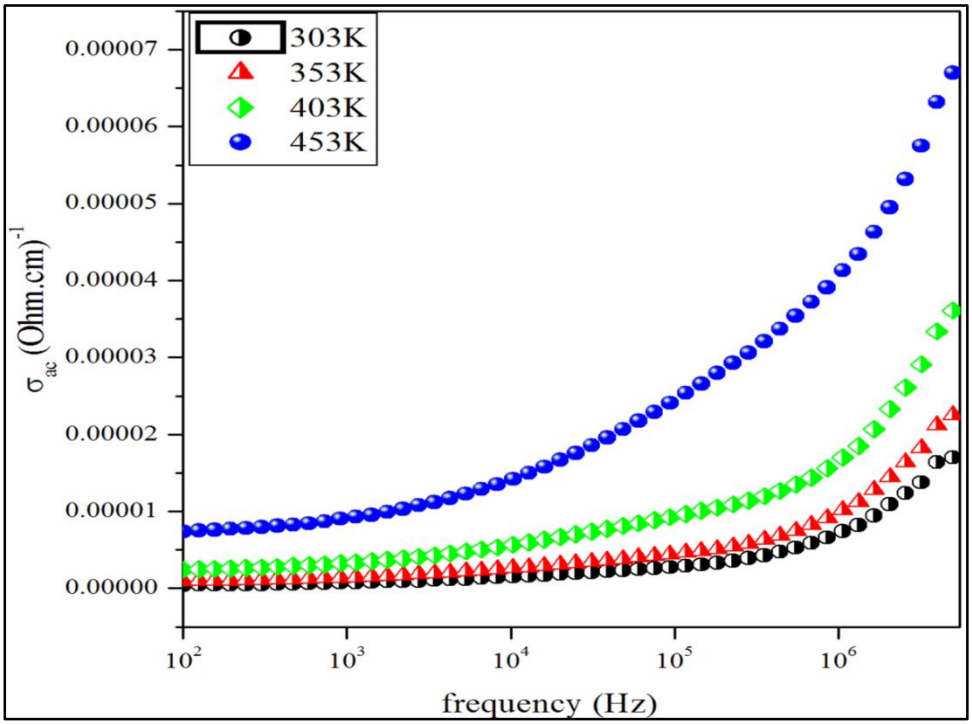

Figure 3.8 Plot of AC conductivity (σ_{ac}) Vs frequency at few selected temperatures for $Ba_4YMn_3O_{11.5-\delta}$ sintered at 1100 ^{0}C for 12 h

The AC conductivity is independent of frequency range of 10^2 - 10^3 Hz after that it increases on increasing temperature. The expression for conductivity is given bellow (equation (3.8))

$$\sigma = \sigma_{dc} + \sigma_{ac} \qquad (3.8)$$

where σ is total conductivity associated with BYMO ceramic, σ_{dc} is the frequency independent part of conductivity and frequency dependent part is ac conductivity (σ_{ac}) which is govern by the following equation (equation (3.9))

$$\sigma_{ac} = A\omega^s \qquad (3.9)$$

Where *A* is constant, ω is angular frequency and *s* is weak function of frequency known as frequency exponent at given temperature. The value of s for BYMO ceramic was found to be 0.324, 0.279, 0.236 and 0.209 at 303, 353, 403 and 453 K, respectively. The value of frequency exponent decreases with increase in temperature. This behavior is only observed in the Correlated Barrier Hopping (CBH) model as proposed by Elliot for crystalline oxide materials. Figure 3.9 shows that the conductivity is nearly constant from 303 - 400 K but after this a prominent increase was observed which indicates at higher temperature material may exhibit semiconducting behavior. It is reported that during sintering diffusion of oxygen takes place between grains and grain boundaries because of difference in partial pressure of oxygen.

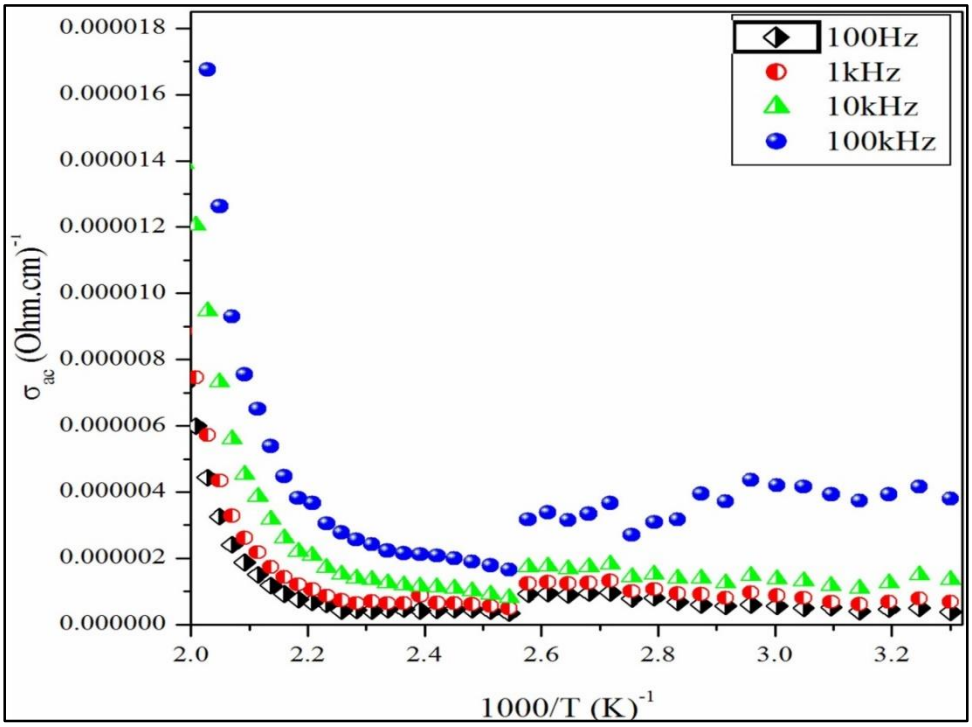

Figure 3.9 Plot of AC conductivity (σ_{ac}) Vs inverse of temperature at certain frequency for $Ba_4YMn_3O_{11.5-\delta}$ sintered at 1100 ^{0}C for 12 h

Grain boundaries shows higher oxygen diffusion rate than grains because grain boundaries possess high oxygen diffusion coefficient. Such effects explain the BYMO material have insulating grain boundaries and semiconducting grains. The insulating grain boundaries acts as barrier for electron transfer between the grains. This increases the charge storage capacity of grains and is explained by internal barrier layer capacitance (IBLC) mechanism. As the temperature increase the resistance of both grain and grain boundaries decreases due to increase of charge transfer between grain and grain boundaries [Varghese and Malhotra (2000)]. The electrical properties of material can be understood by complex plane impedance spectroscopic studies which illustrate the inhomogeneous electrical response due to grain, grain boundary and ceramic interface (electrode) effect. These effect shows well separated relaxations in terms of semicircle arcs on real axis in cole - cole plots. The semicircle corresponding to grain contribution is observed at high frequency followed by semicircles corresponding to grain boundaries and electrode-interface contribution at lower frequency. Figure 3.10 shows the impedance Z" vs. Z’ plots at few selected temperatures. It clearly demonstrates the presence of two semi-circular arcs with different intercepts which may be due to grain boundary and electrode surface effects.

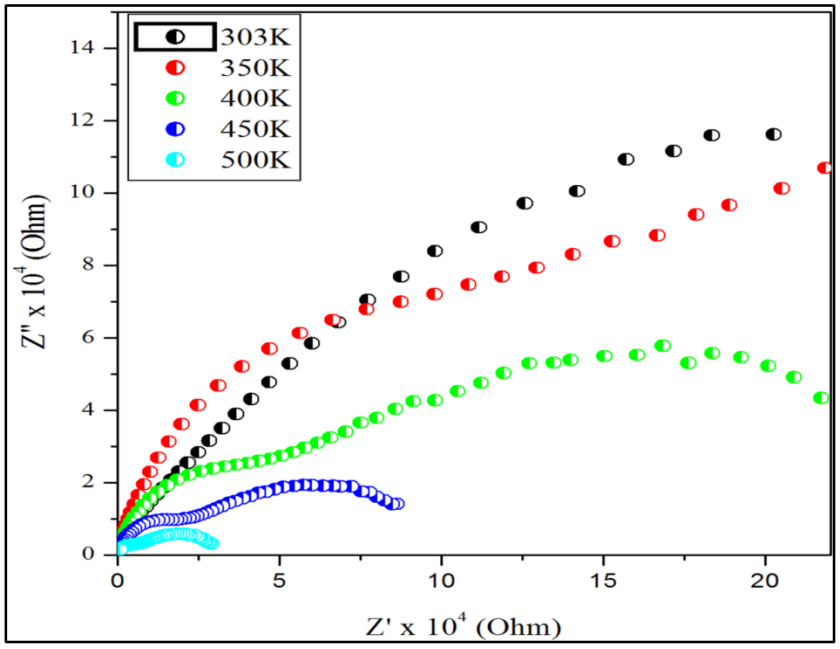

Figure 3.10 Impedance plane plots (Z'' vs Z') at few selected temperatures for $Ba_4YMn_3O_{11.5-\delta}$ sintered at 1100 ^{0}C for 12 h

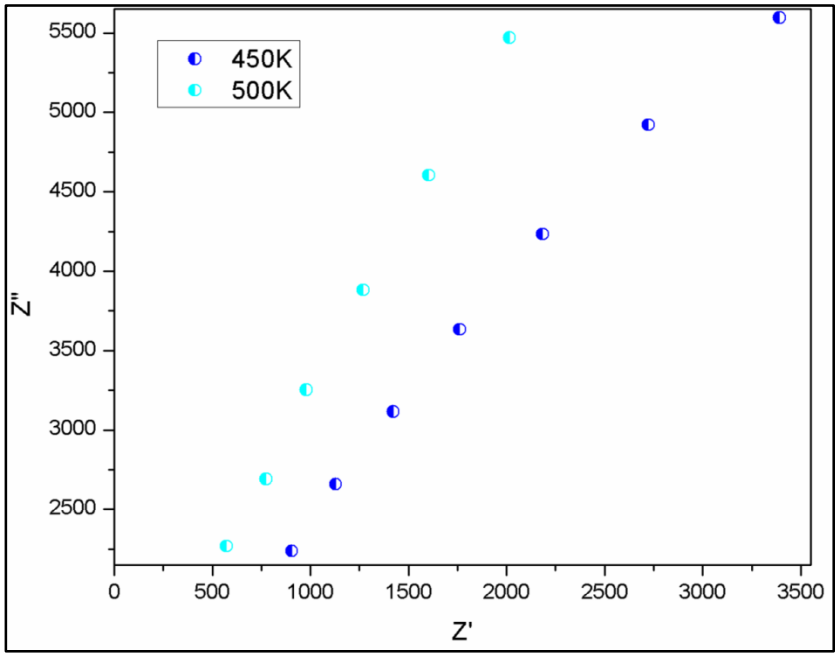

Figure 3.11 An expanded view of impedance plane plot (Z'' Vs Z') of the high frequency region close to the origin at temperatures of 450 and 500 K for $Ba_4YMn_3O_{11.5-\delta}$ sintered at 1100 ^{0}C for 12 h

Figure 3.11 shows the intercept on Z' axis is not found to be zero suggests that there must be existence of another semi-circle in high frequency and at low temperature. The non-zero intercepts on Z' axis is the grain resistance (R_g) and the second semicircle at lower frequency represents the resistance of grain boundary (R_{gb}). Impedance of R_g and R_{gb} calculated by the following formula

$$Z^* = \frac{1}{R_g^{-1} + i\omega C_g} + \frac{1}{R_{gb}^{-1} + i\omega C_{gb}} = Z' - iZ'' \qquad (3.10)$$

where,

$$Z' = \frac{R_g}{1+(\omega R_g C_g)^2} + \frac{R_{gb}}{1+(\omega R_{gb} C_{gb})^2} \qquad (3.11)$$

and

$$Z'' = R_g \left[\frac{\omega R_g C_g}{1+(\omega R_g C_g)^2}\right] + R_{gb} \left[\frac{\omega R_{gb} C_{gb}}{1+(\omega R_{gb} C_{gb})^2}\right] \qquad (3.12)$$

The grain resistance was found to be 8.24×10^2 Ω and 5.03×10^2 Ω at 450 K and 500 K respectively whereas the grain boundary resistance was found to be 8.45×10^4 Ω and 3.05×10^4 Ω at above mentioned temperatures. The grain boundary capacitance was calculated by using the following relation;

$$\omega\tau = 2\pi f_{max} R_{gb} C_{gbb} = 1 \qquad (3.13)$$

Where ω, and τ are angular frequency and relaxation time, respectively. The f_{max} is peak frequency of the impedance semicircle corresponding to grain boundary. The value of C_{gb} was found to be 0.36 μF at 450 K. The grain boundary resistance decreases rapidly as compared to grain resistance. This process is thermally activated so the activation energy (E_a) was calculated by Arrhenius equation;

$$\tau=\tau_0 \, exp^{[-Ea/kBT]} \qquad (3.14)$$

Where, the symbols have their usual meaning. The relaxation time calculated by the relation $\tau=1/2\pi f$.

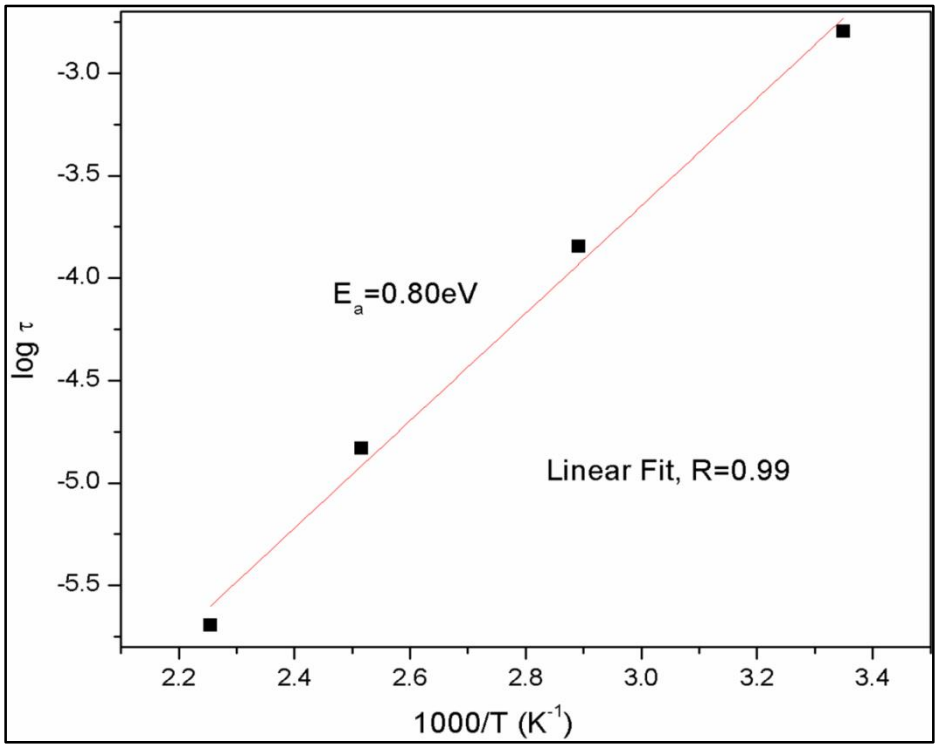

Figure 3.12 Variation of relaxation time τ with inverse of absolute temperature

Figure 3.12 shows the plot of relaxation time (τ) of the grain boundary with the reciprocal of temperature (1000/T). The value of activation energy (E_a) was determined by least square fitting and found to be 0.80 eV which is comparable with reported results of CCTO ceramic [Ni and Chen (2007)].

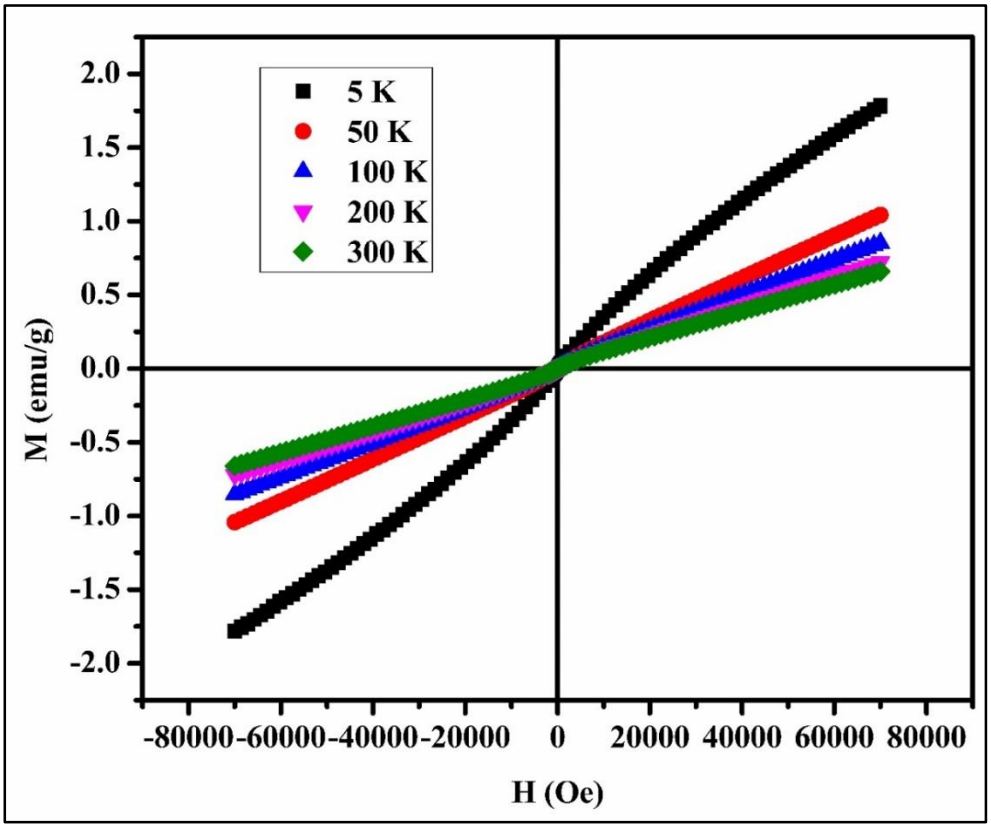

Figure 3.13 M-H hysteresis loop of $Ba_4YMn_3O_{11.5-\delta}$ (BYMO) ceramic

Figure 3.13 shows Magnetization versus magnetic field measured at different temperatures ranging from 5 K to 300 K. The plot exhibits change of remanent (M_r) and coercive (H_c) with increasing temperature. On increasing temperature ferromagnetic character of the material changes towards paramagnetic due to disordering of magnetic domain on increasing temperatures [Agrinskaya *et al*. (2016)].

Temperature dependent magnetization ZFC and FC shown in figure 3.14. On increasing temperature, magnetization decrease gradually and the zero filed cooled (ZFC) and field cooled (FC) is completely coincide which indicates absence of blocking temperature.

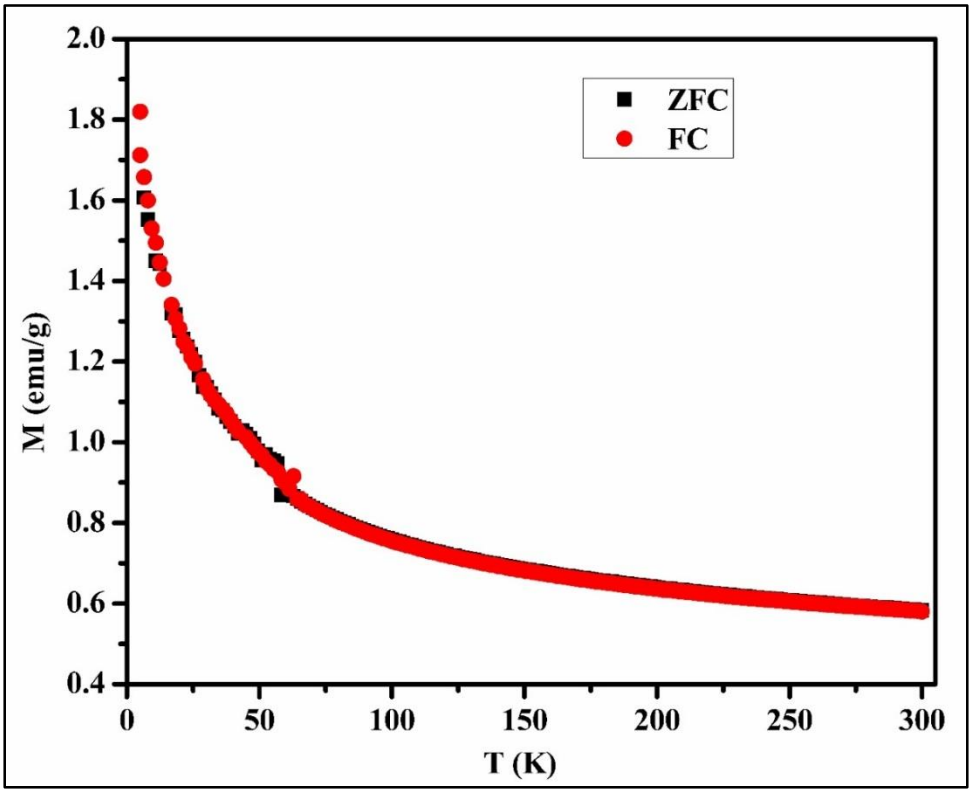

Figure 3.14 Zero field cooled (ZFC) and field cooled (FC) plots of BYMO ceramic

3.4. Conclusion

XRD confirms the single phase formation of BYMO synthesized by chemical route at lower sintering temperature. The material acquired hexagonal perovskite structure confirmed by TEM image and SAED pattern. The dielectric constant gradually increases with decrease in frequency and the increment is prominent in low frequency. The PE hysteresis loop shows ferroelectric nature of material having temperature dependent remanent polarization and coercive field. The value of frequency exponent (s) decreases with increase of temperature this can be explained by Correlated Barrier Hopping (CBH) model. The impedance analysis shows contribution of grains and grain boundaries on dielectric behavior.